Journal of
Materials Chemistry A

Accepted Manuscript

TOC

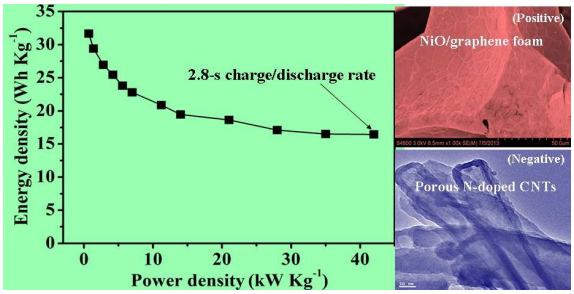

An asymmetric supercapacitor with ultrahigh-rate performance is fabricated using NiO/GF and hierarchical N-doped CNTs as positive and negative electrode, respectively.

Journal of
Materials Chemistry A

Cite this: DOI: 10.1039/c0xx00000x

www.rsc.org/xxxxxx

ARTICLE TYPE

Asymmetric supercapacitors based on nano-architectured nickel oxide/graphene foam and hierarchical porous nitrogen-doped carbon nanotubes with ultrahigh-rate performance

Huanwen Wang, Huan Yi, Xiao Chen, Xuefeng Wang*

Received (in XXX, XXX) Xth XXXXXXXXX 20XX, Accepted Xth XXXXXXXXX 20XX
DOI: 10.1039/b000000x

A pulsed laser deposition process using ozone as an oxidant is developed to grow NiO nanoparticles on highly conductive three-dimensional (3D) graphene foam (GF). The excellent electrical conductivity and interconnected pore structure of the hybrid NiO/GF electrode facilitates fast electron and ion transportion. The NiO/GF electrode displays a high specific capacitance (1225 F g^{-1} at 2 A g^{-1}) and a superb rate capability (68% capacity retention at 100 A g^{-1}). A novel asymmetric supercapacitor with high power and energy densities is successfully fabricated using the NiO/GF as the positive electrode and hierarchical porous nitrogen-doped carbon nanotubes (HPNCNTs) as the negative electrode in aqueous KOH solution. Because of the high individual capacitive performance of the NiO/GF and HPNCNTs, as well as the synergistic effect between the two electrodes, the asymmetric capacitor exhibits excellent energy storage performance. At a voltage range from 0.0 to 1.4 V, an energy density of 32 Wh kg^{-1} is achieved at a power density of 700 W kg^{-1}. Even at a 2.8-s charge/discharge rate (42 kW kg^{-1}), an energy density as high as 17 Wh kg^{-1} is retained. Additionally, the NiO/GF//HPNCNTs asymmetric supercapacitor exhibits excellent cycling durability, with 94% specific capacitance retained after 2,000 cycles.

1. Introduction

As a new class of energy storage devices, supercapacitors are particularly suitable for applications requiring high power density and high charge-discharge rates, such as hybrid vehicles, portable electronic devices and renewable energy systems, because of their much higher power densities than conventional secondary batteries, long cycle-life (up to 104 cycles) and safety tolerance to high rate charge and discharge.[1-3] Unfortunately, the energy storage density of state-of-the-art supercapacitors is limited, generally an order of magnitude lower than that of conventional batteries, which precludes their extensive industrial utilization in energy storage.[4, 5] Although the energy density of supercapacitors can be effectively enlarged using nonaqueous electrolytes,[6-10] a more promising alternative is to use aqueous electrolytes that are more environmentally friendly and have high ionic conductivity, and to enhance the operating potential window by developing asymmetric supercapacitors with a battery type Faradaic electrode as energy source and a capacitive electrode as a power source.[11-13] Asymmetric supercapacitors take the advantage of different potential windows of the two electrodes to increase the device operating voltage and hence improve the energy density.[14]

Up to now, a series of redox-active materials such as transition metal oxides/hydroxides and electrically conducting polymers have been investigated as the positive electrodes in asymmetric supercapacitors.[15] Among them, nickel oxide is of particular interest because of its high theoretical specific capacitance (2583 F g^{-1} within 0.5 V), high chemical/thermal stability, environmentally benign nature, low cost and easy synthesis.[16-18] For example, an asymmetric supercapacitor with NiO as the positive electrode and hierarchical porous carbon as the negative electrode[19] has been demonstrated to exhibit an energy density of 11.6 Wh kg^{-1} at a power density of 28 W kg^{-1}. Nevertheless, like other transition metal oxides, NiO as an electrode material suffers from relatively low electrical conductivity.[20, 21] Recent works have shown nickel oxide coupled with reduced graphene oxide (rGO) for supercapacitor applications.[22-25] Although the pseudocapacitive performances are enhanced in these NiO/rGO composites, the conductivity and specific surface area of graphene are severely impaired in rGO because of abundant defects created during synthesis, as well as aggregation and stacking driven by the strong π-π interaction among graphene sheets. Graphene foams (GF) prepared by chemical vapor deposition (CVD) may avoid these problems because they are 3D continuous and highly conductive graphene network that is free of defects.[26-28] Its high quality and carbonaceous nature provides a highly conductive pathway for electron and ion transportion, which makes graphene foam an ideal 3D interconnected current collector. Thus, it is desirable to construct 3D NiO/GF composites as the positive electrode in asymmetric supercapacitors through a convenient and reliable method.

As for the negative electrode in asymmetric supercapacitors,

activated carbon (AC) is the most widely used materials because of its high surface area and relatively good electrical conductivity. However, the specific capacitance of AC decreases severely with increasing the charging–discharging rate. For instance, AC shows a specific capacitance of only 120 F g^{-1} with an obvious iR drop at 4.8 A g^{-1} in amorphous $Ni(OH)_2$ nanospheres//AC supercapacitor.[29] This has been attributed to the increasing limitation of the inner-pore ion transportion through the small sized tunnels, and consequently the insufficient electrochemical surface accessibility.[30, 31] Therefore, the development of functionalized 3D hierarchical porous carbon nanostructure is highly desirable for high-performance asymmetric supercapacitors.

In the present work, we firstly employ a pulsed laser deposition (PLD) process to prepare a 3D NiO/GF composite, which exhibits an ultrahigh supercapacitive performance. Secondly, functionalized hierarchical porous nitrogen-doped carbon nanotubes (HPNCNTs) are prepared via a facile chemical activation route with polypyrrole (PPy) nanotube as precursor and KOH as activating agent. The HPNCNTs exhibit a high specific capacitance (270 F g^{-1} at 2 A g^{-1} and 182 F g^{-1} at 60 A g^{-1}), and a long cycle life (96% capacitance retention after 6,000 cycles). Finally, an aqueous electrolyte based asymmetric supercapacitor integrating the NiO/GF composite as the positive electrode and HPNCNTs as the negative electrode, has been successfully constructed to demonstrate ultrahigh supercapacitive performance.

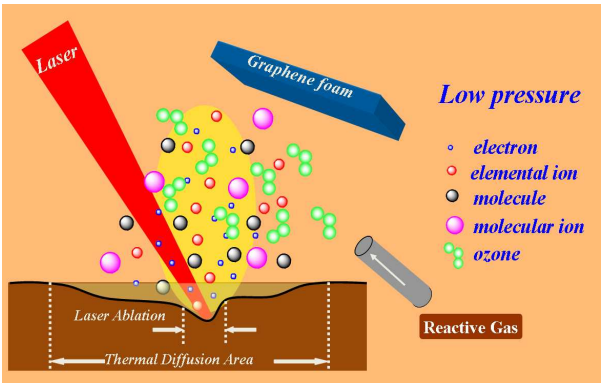

Fig. 1 The PLD process for preparing the NiO/GF.

2. Experiment

2.1 Synthesis of the NiO/GF composite

The GF was prepared as previously reported.[26] The NiO/GF was prepared as follows. The NiO was directly deposited on the GF (1 cm × 1 cm) by the PLD technique inside a stainless steel chamber. Ozone as the oxidizing agent was utilized in the PLD process. It was prepared by tesla coil discharge of pure $16O_2$ in a glass tube and purified by liquid N_2. Before deposition, the chamber was pumped down to a residual pressure of 10^{-4} Pa. The Nd:YAG laser fundamental (1064 nm, 10 Hz repetition rate with 8 ns pulse width) was focused onto a rotating nickel metal target, which generated an energetic atomic beam to react with O_3 gas. The deposition was carried out at room temperature for 1 h. The typical ambient O_3 gas pressure was controlled at 30 Pa by a needle valve. The distance between the target and the substrate was 3 cm.

2.2 Synthesis of the HPNCNTs

The HPNCNTs were synthesized by a two-step process. In the first step, PPy nanotubes were prepared by a reactive template assembly route.[32, 33] 2 mmol methyl orange and 20 mmol $FeCl_3$ were dissolved in 400 mL deionized waterfollowed by adding 20 mmol pyrrole. The solution was kept stirring for 24 h. After stirring, the resultant was isolated by centrifugation, washed for three times with water and ethanol, respectively, and finally dried in a vacuum oven at 60 °C for 24 h. In the second step, functionalized HPNCNTs were fabricated by chemical activation of the PPy precursor with KOH. Briefly, the as-prepared PPy nanotubes (1 g) were dispersed and stirred in KOH solution (20 mL, 3.5 mol L^{-1}) at 60 °C overnight. The resultant mixture was heated up to 850 °C with a heating rate of 3 °C min^{-1} and kept for 1 h under a nitrogen atmosphere. The activated mixtures were washed with dilute HCl solution (1 mol L^{-1}) and deionized water until the filtrate became neutral. The samples were finally dried in a vacuum oven at 60 °C for 24 h.

2.3 Materials Characterization

The products were characterized by field emission scanning electron microscopy (FESEM; Philips XSEM30, Holland), and transmission electron microscopy (TEM; JEOL, JEM-2010, Japan). Raman spectra were collected using a 514 nm laser with RM100 under ambient conditions, with a laser spot size of about 1 mm. X-ray photoelectron spectroscopy (XPS) measurement was performed on a Perkin Elmer PHI 6000C ECSA system with monochromatic Al KR (1486.6 eV) irradiation. Nitrogen adsorption/desorption isotherms were measured at the liquid nitrogen temperature using a Micromeritics Tristar 3000 analyzer.

2.4 Electrochemical Measurements

A three-electrode system was used to measure the electrochemical performance of the NiO/GF and HPNCNTs as the working electrodes in 1 M KOH aqueous solution, with a platinum foil as the counter electrode and Hg/HgO as the reference electrode, respectively. The NiO/GF served directly as the working electrode. The HPNCNTs electrode was prepared by pressing mixtures of the as-prepared HPNCNTs and polytetrafluoroethylene (PTFE) binder (weight ratio of 90:10) onto a piece of carbon fiber paper (1 cm × 1 cm, 0.1 mm thick). The asymmetric supercapacitor was measured with a two-electrode system, where the NiO/GF was the positive electrode, and the HPNCNTs the negative electrode. The loading mass ratio of the active materials (NiO: HPNCNTs) was estimated to be 0.5 from the specific capacitance and the potential window obtained from their galvanostatic charge−discharge curves. The NiO/GF and the HPNCNTs working electrodes were pressed together with a polypropylene membrane as separator. All electrochemical measurements were carried out in 1 M KOH aqueous solution on a CHI660D electrochemical working station.

3. Results and discussion

3.1 Positive Electrode Materials

Fig. 1 briefly shows the PLD process for preparing the NiO/GF electrode. A high energy pulsed laser beam is focused on the rotating nickel target and produces a plasma plume consisting of

the energetic species (such as neutral atoms, molecules, electrons and ions).[34] The ablated species experience multiple collisions with O3 molecules in the deposition chamber to generate nickel oxide molecules in the expanding ablation beam and deposit on the GF. Fig. 2a-d display the FESEM images of GF at different magnifications. From FESEM images of low magnification (Fig. 2a,b), the GF replicates the 3D network and well-defined macroporous structure of Ni foam, without collapsing and cracking. At a higher magnification (Fig. 2c), it is clearly observed that the surface of the graphene skeleton is seamlessly continuous and exhibits micron-scale smooth (flat) topographic domains. Meanwhile, ripples and wrinkles are formed on the graphene due to the difference between the thermal expansion coefficients of nickel and graphene (Fig. 2d). The optical image of GF and NiO/GF is shown in Fig. 2e. Apparently, NiO can be grown on GF on a large scale. Similar to GF (Fig. 2e), the hybrid material completely preserves the 3D interconnected network structure of the GF. Each strip of the GF is evenly covered by the NiO nanoparticles. Closer FESEM observation (Fig. 2f) reveals that these NiO nanoparticles are uniform in size, which ensures a short electrolyte ion diffusion length.

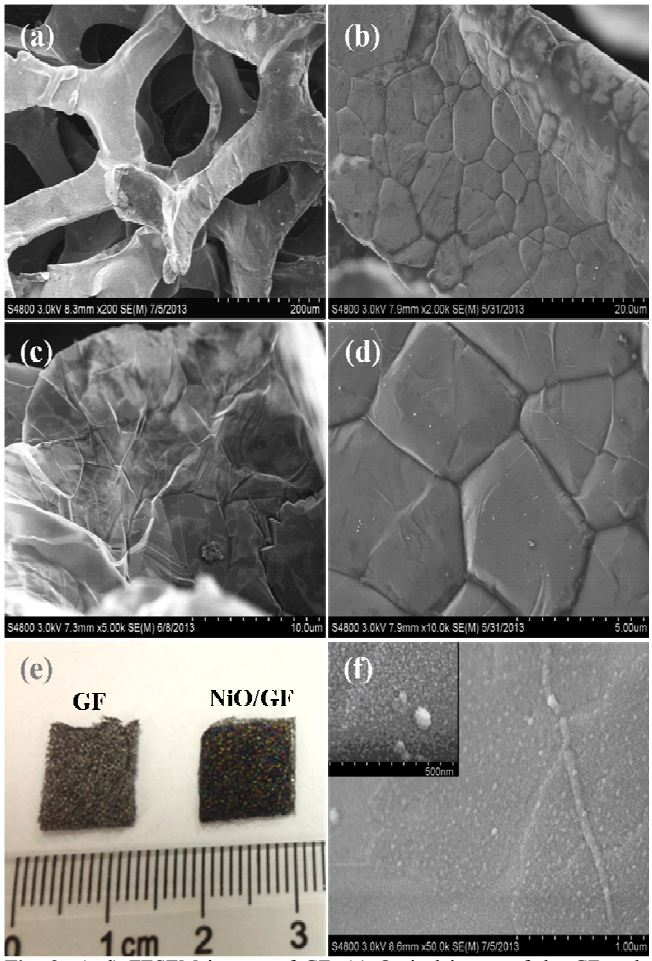

Fig. 2 (a-d) FESEM images of GF. (e) Optical image of the GF and NiO/GF. (f) FESEM images of the NiO/GF.

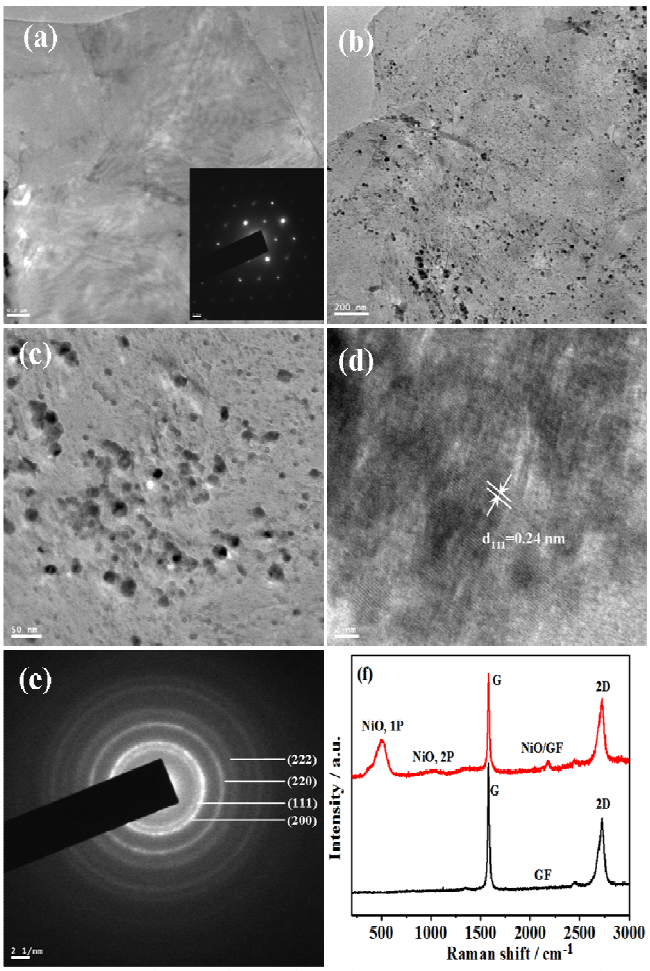

Fig. 3 (a) TEM image of a graphene sheet. Inset: SAED pattern. (b, c) TEM and (d) HRTEM images of the NiO/GF. (e) SAED pattern of the NiO particle in NiO/GF. (f) Raman spectra of the GF and NiO/GF. Scale bars, 0.2 μm (a); 200 nm (b); 50 nm (c); 2 nm (d).

TEM measurements are carried out to further investigate the microstructure of the GF and NiO/GF. Fig. 3a shows the TEM image of a graphene sheet of large size. The selected area electron diffraction (SAED) pattern (inset of Fig. 3a) gives reflection spots arranged in a typical hexagonal pattern, confirming the formation of high-quality graphene.[35] The TEM images of Fig 3b,c show that NiO nanoparticles (approximately 20 nm in size) are uniformly distributed on graphene sheets. The high-resolution TEM (HRTEM) image of the NiO reveals typical regular lattice fringes with the d spacing of 0.24 nm, corresponding to the (111) plane of NiO (Fig. 3d). The SAED pattern (Fig. 3e) displays well-defined diffraction rings, suggesting the polycrystalline characteristic that can be indexed to the NiO crystal structure (JCPDS No. 47-1049).

We also perform Raman analysis (Fig. 3f) to further investigate the structure of the GF and NiO/GF. The absence of Raman D band indicates that the grown graphene is of high quality, which ensures a high conductivity of 3D GF. The presence of the G peak at 1580 cm^{-1}, the 2D peak at 2726 cm^{-1} and the G/2D ratio reveal the typical Raman characteristics for few-layer graphene sheets, which is similar to those reported for CVD grown graphene layers.[36, 37] In comparison with 3D graphene networks, the NiO/GF exhibits two additional Raman peaks, i.e., a sharp

peak at ~510 cm^{-1} and a broad one at ~1040 cm^{-1}, which can be assigned to the first- (1P) and second-order phonon (2P) scattering, respectively, in NiO.[38, 39] The Raman results further suggest the successful integration of the NiO particles and GF.

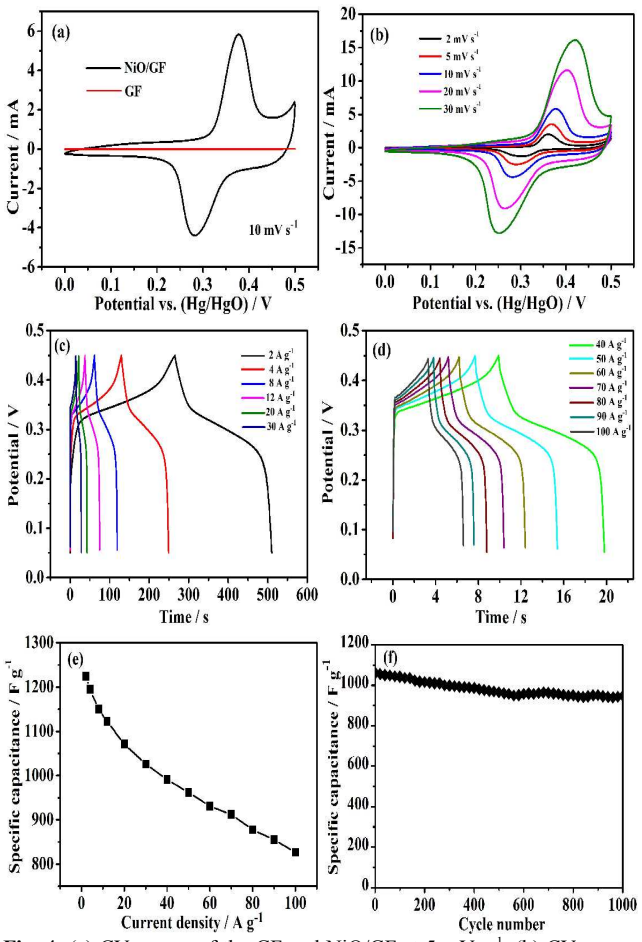

Fig. 4 (a) CV curves of the GF and NiO/GF at 5 mV s^{-1}. (b) CV curves of the NiO/GF at different sweep rates. (c, d) Galvanostatic charge–discharge curves of the NiO/GF at different current densities. (e) Capacitance values versus current densities. (f) Cycling performance of the NiO/GF at 12 A g^{-1} for 1000 cycles.

The pseudocapacitive properties of the NiO/GF electrode are analyzed using cyclic voltammetry (CV) and galvanostatic charge–discharge (CD) measurements in a three-electrode system. Fig. 4a shows typical CV curves of GF and NiO/GF from 0 to 0.5 V at 5 mV s^{-1}. As can be seen, GF exhibits negligible capacitive current. By contrast, the current is dramatically enhanced by introduction of NiO onto 3D GF. The CV curve of the NiO/GF consists of a pair of redox peaks, $NiO + OH^- \leftrightarrow NiOOH + e^-$, at $E_{1/2}$ = 0.33 V ($E_{p,a}$ = 0.38 V, $E_{p,c}$ = 0.28 V) consistent with the capacitance characteristics of Faradaic processes. The peak separation of this redox couple (100 mV) is much lower than that of NiO/Ni nanocomposites,[16] NiO nanocolumns[40] and NiO Nanobelts,[41] indicating an excellent electrochemical reversibility of the NiO/GF electrode. Increasing the scan rate leads to further augment of the CV curve and the redox peaks (Fig. 4b), indicating rapid charge transport from NiO to GF.

Fig. 4c,d exhibits a set of CD curves for the NiO/GF electrode at different current densities. Note that the tested current densities are in the high-current density range when referring to the literature. The specific capacitance can be calculated based on discharge curves. Fig. 4e illustrates the relationship between specific capacitance and current density. The specific capacitance of the NiO/GF is as high as 1225 F g^{-1} at a current density of 2 A g^{-1} and retains 827 F g^{-1} (68%) at 50 times greater current density (100 A g^{-1}). To the best of our knowledge, such high specific capacitance and good rate capability are superior to any results reported for NiO in the literature.[16, 39-41] In addition, the NiO/GF electrode retains 89% capacitance over 1,000 cycles (Fig. 4f). This superior peudocapacitive performance may be attributable to several factors. Firstly, the highly conductive and microporous GF as current collector can not only provide a continuous electron transfer pathway, but also facilitate ion transportation by shortening diffusion distance. Secondly, the ablated species with high excitation energy (up to a few keV) are directly deposited on GF with robust adhesion, which could reduce the contact resistance at the interface between the GF current collector and active materials. Finally, the direct contact of NiO nanoparticles with the GF substrate avoids the use of polymer binders and conductive additives, and substantially reduces the "dead volume" in the electrode.

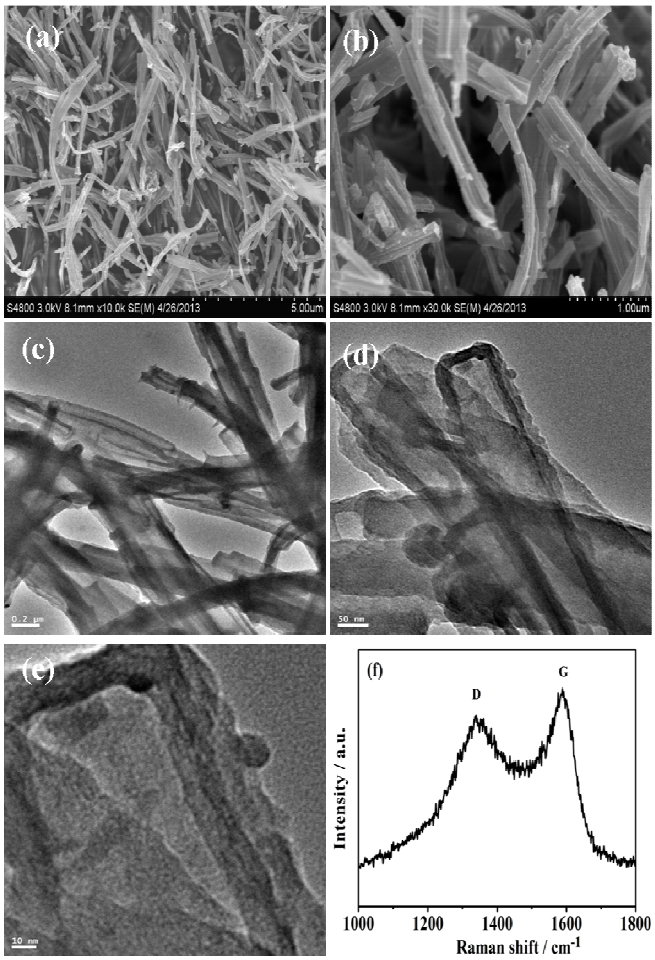

Fig. 5 (a, b) FESEM, (c, d) TEM, (e) HRTEM images and (f) Raman spectrum of the HPNCNTs. Scale bars, 0.2 μm (c); 50 nm (d); 10 nm (e).

3.2 Negative Electrode Materials

Most of the researches on supercapacitors are dedicated to the

positive electrode materials while the negative electrode materials are rarely studied. For development of high-performance carbon-based negative materials in asymmetric supercapacitors, challenges exist for achieving large specific surface area, high conductivity, efficient porosities in micro-, meso- or macropores, 3D nano-architecture and high-level heteroatomdoping. Herein, functionalized 3D HPNCNTs are fabricated as the negative materials via a chemical activation route with PPy nanotubes as precursor. The morphology of PPy is shown in Fig. S1. FESEM images present the fibrillar feature of PPy (Fig. S1ab). The TEM images in Fig. S1c,d clearly demonstrate the tubular structure with approximately 190 nm in outer diameter and 120 nm in inner diameter. The PPy is chemically activated with KOH at 850 °C under a nitrogen atmosphere, leading to formation of HPNCNTs with the same morphology of the PPy template (Fig. 5a,b). However, HPNCNTs have much lower outer diameter (130 nm) and inner diameter (70 nm) due to the weight loss (Fig. 5c,d). It is suggested that the activation of PPy with KOH proceeds as $6KOH + C \rightarrow 2K + 3H_2 + 2K_2CO_3$, followed by decomposition of K_2CO_3 and/or reaction of $K/K_2CO_3/CO_2$ with Ppy.[42] The Raman spectrum (Fig. 5f) clearly shows the well-known D-band peak at ~1342 cm^{-1} and G-band at ~1589 cm^{-1}. The strong D-band peak indicates that HPNCNTs have a low degree of graphitization and contains a significant amount of disordered sections and defects, which is also confirmed by HRTEM image in Fig. 5e.

The activation with KOH could generate nanoscale pores in the resultant carbon. To probe the porous structure of HPNCNTs, nitrogen adsorption–desorption isotherms are measured (Fig. 6). Significant hysteresis characteristics of the isotherms at high relative pressures (0.45–1.0) indicate the existence of abundant mesopores. The specific Brunauer–Emmett–Teller (BET) surface area reaches as high as 2,080 $m^2 g^{-1}$ with a pore volume (BJH model) up to 1.23 $m^3 g^{-1}$. The pore size distribution is shown in the inset of Fig. 6. It can be seen that HPNCNTs possess both mesopores peaked at 3.71 nm and micropores peaked at 1.89 nm.

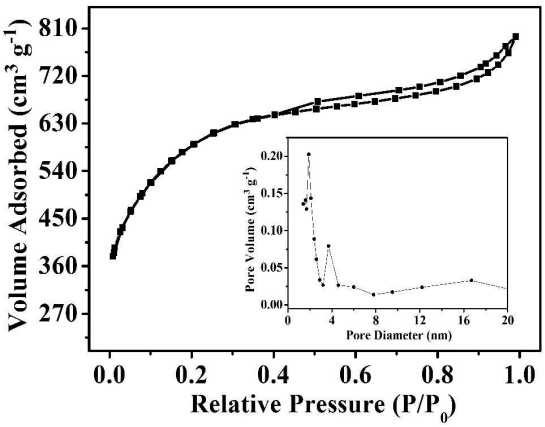

Fig. 6 Nitrogen adsorption and desorption isotherms measured at 77 K for the HPNCNTs. The inset shows the corresponding BJH pore size distribution.

Elemental analysis indicates that the N and O contents in THPC are 2.8 wt% and 12.4 wt%, respectively. To evaluate the chemical identities of the heteroatom in HPNCNTs, XPS measurement is carried out. As shown in Fig. 7a, HPNCNTs show a predominant C 1s peak at around 284.8 eV, a weak O 1s peak at around 532.0 eV, and a pronounced N 1s peak at around 400.0 eV, the latter verifies the doping of N atoms in HPNCNTs. The N 1s spectrum (Fig. 7b) can be fitted by a set of peaks located at 401.5, 400.3 and 398.3 eV for quaternary, pyrrolic, and pyridinic nitrogen, respectively.[43] This indicates that the N atoms within the pentagonal ring of PPy are partly converted into quaternary or pyridinic nitrogen during the carbonization process.

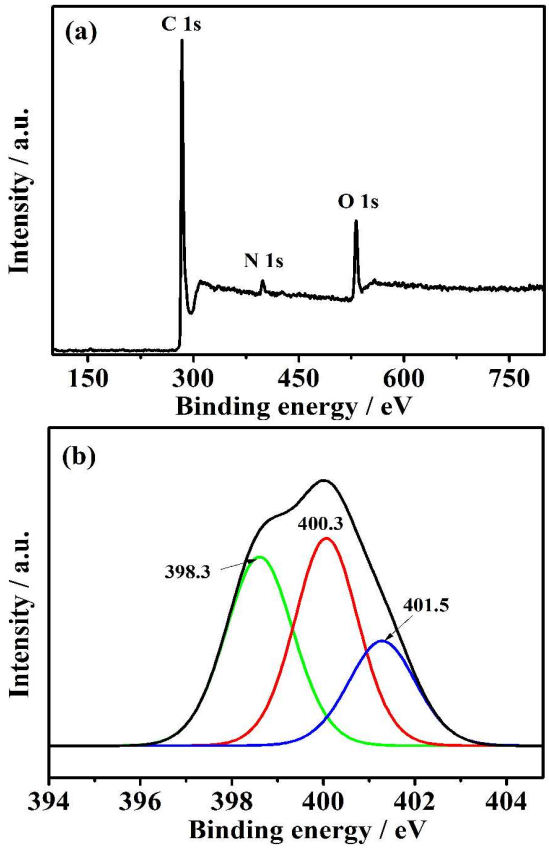

Fig. 7 XPS spectra of (a) HPNCNTs and (b) the corresponding high-resolution N1s peak.

Fig. 8a,b shows typical CV curves of HPNCNTs at various scan rates from 5 to 500 mV s^{-1}. Over this wide range of scan rates, the shapes of these curves are quasi-rectangular, indicating an ideal capacitive behavior and fast diffusion of electrolyte ions into the electrode. Fig. 8c,d exhibit the CD curves of HPNCNTs at different current densities from 2 A g^{-1} to 60 A g^{-1}. All these curves are highly linear and symmetrical, indicating an excellent electrochemical reversibility. The specific capacitance of HPNCNTs is up to 270 F g^{-1} at 2 A g^{-1} (Fig. 8e). Even at 60 A g^{-1}, the specific capacitance is still as high as 182 F g^{-1}. Furthermore, after 6,000 cycles at a scan rate of 500 mV s^{-1}, the capacitance remains 96% of its initial value, indicative of a good electrochemical stability of HPNCNTs. This superior capacitive behavior is resulted from the unique microstructure of HPNCNTs: (i) abundant micro- and mesopores which provides a high surface area, resulting in a large capacitance; (ii) the nanotube architecture which provides a short diffusion distance and more ion channels to facilitate ion transportation; (iii) nitrogen doping which enhances the electrical conductivity, the wettability and the

reactivity.

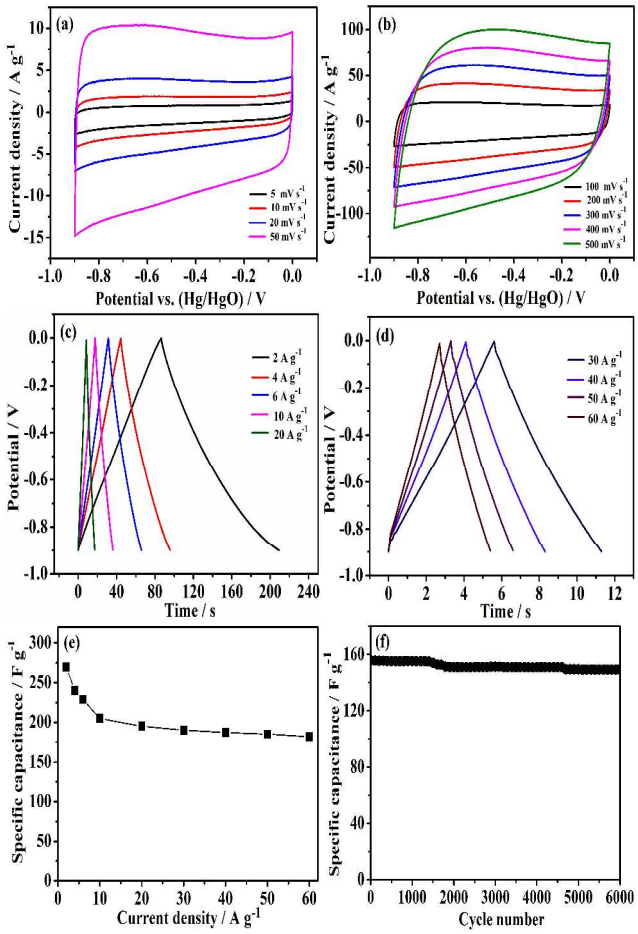

Fig. 8 (a, b) CV curves of HPNCNTs at different sweep rates. (c, d) Galvanostatic charge–discharge curves of HPNCNTs at different current densities. (e) Capacitance values versus current densities. (f) Cycling performance of HPNCNTs at 500 mV s^{-1} for 6000 cycles.

3.3 Asymmetric Supercapacitors

On the basis of the potential window for NiO/GF (0.0 ~ 0.5 V) and HPNCNTs (-0.9 ~ 0.0 V), with regard to the Hg/HgO, the operating cell voltage is expected to be extended to approximately 1.4 V in a NiO/GF//HPNCNTs asymmetric supercapacitor. To obtain a well electrochemical performance, the charge balance between the two electrodes should follow the relationship $q^{+} = q^{-}$.[44] The stored charge is related to the specific capacitance (C), the potential window in the charge−discharge process (ΔV), and the mass of the electrode (m), which follows the equation: $q = C \times \Delta V \times m$. According to the above analysis of the specific capacitance value and potential window for the NiO/GF and HPNCNTs, the optimal mass ratio between the two electrodes is expected to be mNiO/GF/mHPNCNTs = 0.5 in an asymmetric supercapacitor.

Fig. 9a presents typical CV curves for the NiO/GF//HPNCNTs-based supercapacitor in 1 M KOH aqueous solution at various scan rates between 0.0 and 1.4 V. Two broad redox peaks were observed indicating the Faradaic pseudocapacitive nature of the NiO/GF//HPNCNTs capacitor arising from the NiO/GF electrode. The galvanostatic CD curves at different current densities from 2 A g^{-1} to 60 A g^{-1} are shown in Fig. 9b,c. No obvious iR drop is observed for any of these curves, indicating a low internal resistance for the asymmetric supercapacitor. Additionally, all the discharge curves are nearly symmetric to their corresponding charging counterparts, suggesting an excellent electrochemical reversibility and a good coulombic efficiency. The relationship between specific capacitance (based on the total mass of the active materials of the two electrodes) and current density is illustrated in Fig. 9d. The specific capacitance reaches a maximum of 116 F g^{-1} at 1 A g^{-1} and retains 61 F g^{-1} at a high current density of 60 A g^{-1} (a full charge-discharge within 2.8 s). Fig. 9e shows the cycle performance of the NiO/GF//HPNCNTs asymmetric supercapacitor measured at a current density of 10 A g^{-1} for 2,000 cycles. The capacitance retention after 2,000 cycles of charge/discharge is 94%, indicating an excellent long-term stability of the asymmetric supercapacitor. This cycling performance is superior to most of previous reported samples including $Ni(OH)_2$//AC (82% retention after 1000 cycles),[45] graphene/MnO_2//graphene (79% retention after 1000 cycles),[44] $NiCo_2O_4$−rGO//AC (83% after 2500 cycles),[46] and Ni−Co oxide//AC (85% after 2000 cycles).[47] The excellent capacitive performance of the fabricated NiO/GF//HPNCNTs asymmetric supercapacitor could be reasonably attributed to the synergistic effect between the positive and negative electrodes.

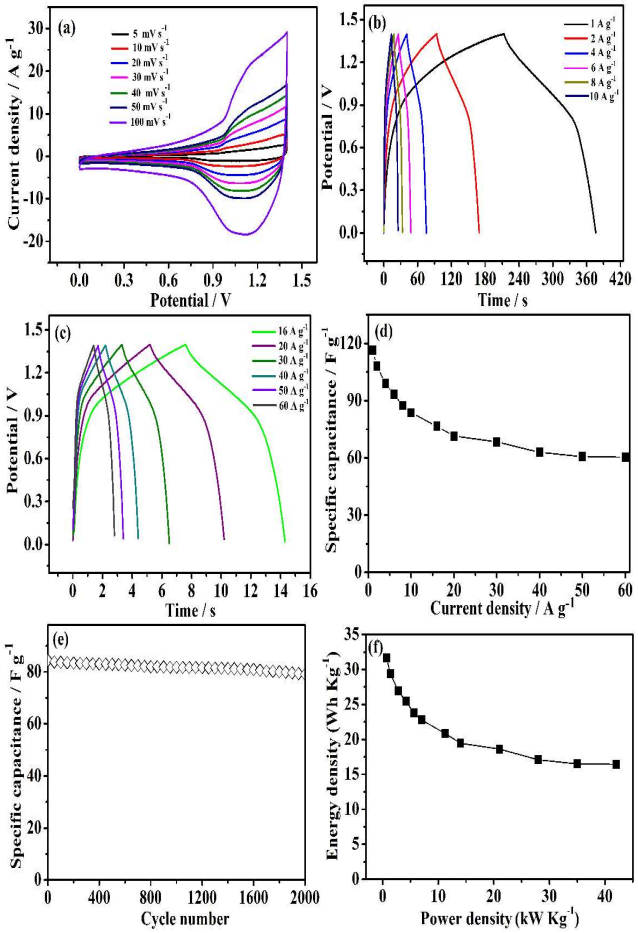

Fig. 9 Electrochemical characterization of the NiO/GF//HPNCNTs asymmetric supercapacitor. (a) CV curves of the NiO/GF//HPNCNTs asymmetric supercapacitor at various scan rates in 1M KOH. (b, c) Galvanostatic charge–discharge curves of the capacitor at various current

densities (ranging from 1 to 60 A g^{-1}). (c) Specific capacitance of the asymmetric supercapacitor as a function of current density. (d) Cycle performance of the asymmetric supercapacitor measured at 10 A g^{-1} for 2000 cycles. (e) Energy and power density of the NiO/GF//HPNCNTs asymmetric supercapacitor.

The energy density and power density are two important parameters that characterize the performance of supercapacitors. Fig. 9f is a Ragone plot, which correlates the energy density and the power density of the NiO/GF//HPNCNTs asymmetric supercapacitor. The energy density of the supercapacitors decreases from 32 to 17 Wh kg^{-1} as the power density increases from 0.7 to 42 kW kg^{-1}. This is much higher than that of a symmetric supercapacitor based on HPNCNTs//HPNCNTs (e.g., 3 Wh kg^{-1} at 12 kW kg^{-1}) (Fig. S2). It also outperforms most of asymmetric supercapacitors in the literature such as $Ni(OH)_2$/graphene//porous graphene (13.5 Wh kg^{-1} at 15.2 kW kg^{-1}),[15] graphene/$Ni(OH)_2$//graphene/RuO_2 (14 Wh kg^{-1} at 21 kW kg^{-1}),[48] graphene/MnO_2//graphene (7 Wh kg^{-1} at 5 kW kg^{-1}),[44] CoO@PPy nanowire array//AC (11.8 Wh kg^{-1} at 5.5 kW kg^{-1}),[49] Graphene-$NiCo_2O_4$//AC (7.6 Wh kg^{-1} at 5.6 kW kg^{-1}), [50] graphene/MnO_2//ACN (8.2 Wh kg^{-1} at 16.5 kW kg^{-1}),[51] and RGO–RuO_2//RGO–PANi (6.8 Wh kg^{-1} at 49.8 kW kg^{-1}).[52] Most importantly, the highest power density, 42 kW kg^{-1}, can meet the power demands of the PNGV (Partnership for a New Generation of Vehicles),[53-56] demonstrating great potential of NiO/GF//HPNCNTs asymmetric supercapacitors as power supply components in hybrid vehicle systems.

It should be noted that there is an IR drop in HPNCNTs electrodes both the three electrode and symmetric cell charge-discharge (Fig. 8d, S2d), but in the asymmetric cell there is no such IR drop observed. This difference may be related with the electrode microstructure. The HPNCNTs electrode is prepared by pressing mixtures of the as-prepared HPNCNTs and polytetrafluoroethylene (PTFE) binder (weight ratio of 90:10) onto a piece of carbon fiber paper. Usually, as for traditional slurry-coating technique, a large portion of electroactive surface of electrode materials is blocked from contact with the electrolyte. Furthermore, the polymer binder included will greatly decrease the electrical conductivity of the electrode materials, hence showing an IR drop in HPNCNTs electrodes with both three electrode and symmetric cell. Comparatively, NiO particles are directly grown on 3D continuous and highly conductive graphene network, which can be self-supported and binder-free electrodes. When the NiO/GF and the HPNCNTs electrodes are pressed together to form the asymmetric cell, no obvious IR drop is observed. In addition, from the EIS analysis (Fig. S3), it is clear that the imaginary part of the impedance curves approaches a vertical line at low frequency, implying an ideal capacitive behavior of the the NiO/GF//HPNCNTs asymmetric supercapacitor.[57]

4. Conclusions

In summary, a novel and ultrahigh-rate asymmetric supercapacitor based on NiO/GF and HPNCNTs materials as the positive and negative electrodes, respectively, has been developed in aqueous KOH solution. The as-assembled NiO/GF//HPNCNTs asymmetric supercapacitor shows high specific capacitance, high energy density, high power density and good cycling stability at an operating voltage of 1.4 V. In particular, an energy density of 17 Wh kg^{-1} has been obtained at an ultrahigh power density of 42 kW kg^{-1} (a full charge-discharge within 2.8 s), which surpasses most of the other previously reported metal (Co, Ni, Mn) oxide-based asymmetric supercapacitors. The NiO/GF//HPNCNTs supercapacitor is expected to be a highly promising candidate for application in high-performance energy storage systems.

Acknowledgements

The authors gratefully acknowledge the financial support offered by NSFC Grant (21173158) and STCSM (10PJ1409600).

Notes and references

Department of Chemistry, Key Laboratory of Yangtze River Water Environment, Ministry of Education, Tongji University, Shanghai 200092, China. Fax: 86-21-65981097; Tel: 86-21-65981097; E-mail: xfwang@tongji.edu.cn

†Electronic Supplementary Information (ESI) available: Calculations of specific capacitance, energy density and power density based on the galvanostatic charge–discharge curves. FESEM and TEM images of PPy nanotubes. Electrochemical characterization of the HPNCNTs//HPNCNTs symmetric supercapacitor: See DOI: 10.1039/b000000x/

1 P. Simon and Y. Gogotsi, *Nat. Mater.* 2008, **7**, 845.
2 G. Yu, L. Hu, N. Liu, H. Wang, M. Vosgueritchian, Y. Yang, Y. Cui and Z. Bao, *Nano Lett*. 2011, **11**, 4438.
3 H. Wang, H. S. Casalongue, Y. Liang and H. Dai, *J. Am. Chem. Soc*., 2010, **132**, 7472.
4 Q. Qu, S. Yang and X. Feng, *Adv. Mater*. 2011, **23**, 5574.
5 T. Y. Wei, C. H. Chen, H. C. Chien, S. Y. Lu and C. C. Hu, *Adv. Mater*. 2010, **22**, 347.
6 M. F. El-Kady, V. Strong, S. Dubin and R. B. Kaner, *Science* 2012, **335**, 1326.
7 H. Wang, Y. Wang and X. Wang, *New J. Chem*. 2013, **37**, 869.
8 C. M. Ionica-Bousquet, W. J. Casteel, R. M. Pearlstein, G. GirishKumar, G. P. Pez, P. Gomez-Romero, M. R. Palacin and D. Munoz-Rojas, *Electrochem. Commun*. 2010, **12**, 636.
9 H. J. Liu, W. J. Cui, L. H. Jin, C. X. Wang and Y. Y. Xia, *J. Mater. Chem*. 2009, **19**, 3661.
10 E. Frackowiak, *Phys. Chem. Chem. Phys*. 2007, **9**, 1774.
11 Z. Tang, C. Tang and H. Gong, *Adv. Funct. Mater*. 2012, **22**, 1272.
12 X. Lu, M. Yu, G. Wang, T. Zhai, S. Xie, Y. Ling, Y. Tong and Y. Li, *Adv. Mater*. 2013, **25**, 267.
13 C. C. Hu, J. C. Chen and K. H. Chang, *J. Power Sources* 2013, **221**, 128.
14 X. Lu, M. Yu, T. Zhai, G. Wang, S. Xie, T. Liu, C. Liang, Y. Tong and Y. Li, *Nano Lett*. 2013, **13**, 2628.
15 J. Yan, Z. Fan, W. Sun, G. Ning, T. Wei, Q. Zhang, R. Zhang, L. Zhi and F. Wei, *Adv. Funct. Mater*. 2012, **22**, 2632.
16 Q. Lu, M. W. Lattanzi, Y. Chen, X. Kou, W. Li, X. Fan, K. M. Unruh, J. G. Chen and J. Q. Xiao, *Angew. Chem*. 2011, **123**, 6979.
17 F. Luan, G. Wang, Y. Ling, X. Lu, H. Wang, Y. Tong, X. X. Liu and Y. Li, *Nanoscale*, 2013, **5**, 7984.
18 M. S. Wu, M. J. Wang and J. J. Jow, *J. Power Sources* 2010, **195**, 3950.
19 D. W. Wang, F. Li and H. M. Cheng, *J. Power Sources* 2008, **185**, 1563.
20 J. Jiang, J. Liu, W. Zhou, J. Zhu, X. Huang, X. Qi, H. Zhang and T. Yu, *Energy Environ. Sci*., 2011, **4**, 5000.
21 J. Y. Kim, S. H. Lee, Y. Yan, J. Oh and K. Zhu, *RSC Advances*, 2012, **2**, 8281.
22 W. Lv, F. Sun, D. M. Tang, H. T. Fang, C. Liu, Q. H. Yang and H. M. Cheng, *J. Mater. Chem*., 2011, **21**, 9014.
23 Y. Y. Yang, Z. A. Hu, Z. Y. Zhang, F. H. Zhang, Y. J. Zhang, P. J. Liang, H. Y. Zhang and H. Y. Wu, *Mater. Chem. Phys*. 2012, **133**, 363.
24 M. S. Wu,Y. P. Lin, C. H. Lin and J. T. Lee, *J. Mater. Chem*., 2012, **22**,

2442.
25 B. Zhao, J. Song, P. Liu, W. Xu, T. Fang, Z. Jiao, H. Zhang and Y. Jiang, *J. Mater. Chem*., 2011, **21**, 18792.
26 Z. Chen, W. Ren, L. Gao, B. Liu, S. Pei and H. M. Cheng, *Nat. Mater*. 2011, **10**, 424.
27 X. C. Dong, H. Xu, X. W. Wang, Y. X. Huang, M. B. Chan-Park, H. Zhang, L. H. Wang, W. Huang and P. Chen, *ACS Nano* 2012, **6**, 3206.
28 H. Ji, L. Zhang, M. T. Pettes, H. Li, S. Chen, L. Shi, R. Piner and R. S. Ruoff, *Nano Lett*. 2012, **12**, 2446.
29 H. B. Li, M. H. Yu, F. X. Wang, P. Liu, Y. Liang, J. Xiao, C. X. Wang, Y. X. Tong and G. W. Yang, *Nat. Commun*. 2013, **4**, 1894.
30 L. Qie, W. M. Chen, Z. H. Wang, Q. G. Shao, X. Li, L. X. Yuan, X. L. Hu, W. X. Zhang and Y. H. Huang, *Adv. Mater*. 2012, **24**, 2047.
31 L. Qie, W. Chen, H. Xu, X. Xiong, Y. Jiang, F. Zou, X. Hu, Y. Xin, Z. Zhang and Y. Huang, *Energy Environ. Sci*., 2013, **6**, 2497.
32 X. M. Yang, Z. X. Zhu, T. Y. Dai and Y. Lu, *Macromol. Rapid Commun*. 2005, ***26***, 1736.
33 H. Yoon, M. Chang and J. Jang, *J. Phys. Chem. B*, 2006, **110**, 14074.
34 D. H. Lowndes, D. B. Geohegan, A. A. Puretzky, D. P. Norton and C. M. Rouleau, *Science*, 1996, **273**, 898.
35 J. C. Meyer, A. K. Geim, M. I. Katsnelson, K. S. Novoselov, T. J. Booth and S. Roth, *Nature* 2007, **446**, 60.
36 Y. He, W. Chen, X. Li, Z. Zhang, J. Fu, C. Zhao and E. Xie, *ACS Nano* 2013, **7**, 174.
37 W. Wang, S. Guo, M. Penchev, I. Ruiz, K. N.Bozhilov, D. Yan, M. Ozkan and C. S. Ozkan, *Nano Energy* 2013, **2**, 294.
38 H. Wang, H. Yi, X. Chen and X. Wang, *Electrochim. Acta* 2013, **105**, 353.
39 X. Cao, Y. Shi, W. Shi, G. Lu, X. Huang, Q. Yan, Q. Zhang and H. Zhang, *Small* 2011, **7**, 3163.
40 X. Zhang, W. Shi, J. Zhu, W. Zhao, J. Ma, S. Mhaisalkar, T. L. Maria, Y. Yang, H. Zhang, H. H. Hng and Q. Yan, *Nano Res*. 2010, **3**, 643.
41 B. Wang, J. S. Chen, Z. Wang, S. Madhavi, X. W. Lou and *Adv. Energy Mater*. 2012, **2**, 1188.
42 Y. Zhu, S. Murali, M. D. Stoller, K. J. Ganesh, W. Cai and P. J. Ferreira, A. Pirkle, R. M. Wallace, K. A. Cychosz, M. Thommes, D. Su, E. A. Stach and R. S. Ruoff, *Science* 2011, **332**, 1537.
43 L. F. Chen, X. D. Zhang, H. W. Liang, M. Kong, Q. F. Guan, P. Chen, Z. Y. Wu and S. H. Yu, *ACS Nano*, 2012, **6**, 7092.
44 Z. S. Wu, W. Ren, D. W. Wang, F. Li, B. Liu and H. M. Cheng, *ACS Nano* 2010, **4**, 5835.
45 J. W. Lang, L. B. Kong, M. Liu, Y. C. Luo and L. Kang, *J. Solid State Electron*. 2010, **14**, 1533.
46 X. Wang, W. S. Liu, X. H. Lu and P. S. Lee, *J. Mater. Chem*. 2012, **22**, 23114.
47 C. H. Tang, Z. Tang and H. Gong, *J. Electrochem. Soc*. 2012, **159**, A651.
48 H. Wang, Y. Liang, T. Mirfakhrai, Z. Chen, H. S. Casalongue and H. Dai, *Nano Res*. 2011, **4**, 729.
49 C. Zhou, Y. Zhang, Y. Li and J. Liu, *Nano Lett*. 2013, **13**, 2078.
50 H. Wang, C. M. B. Holt, Z. Li, X. Tan, B. S. Amirkhiz, Z. Xu, B. C. Olsen, T. Stephenson and D. Mitlin, *Nano Res*. 2012, **5**, 605.
51 Z. Fan, J. Yan, T. Wei, L. Zhi, G. Ning, T. Li and F. Wei, *Adv. Funct. Mater*. 2011, **21**, 2366.
52 J. Zhang, J. Jiang, H. Li and X. S. Zhao, *Energy Environ. Sci*., 2011, **4**, 4009.
53 B. Scrosati, *Nature* 1995, **373**, 557.
54 R. F. Nelson, *J. Power Sources* 2000, **91**, 2.
55 D. W. Wang, F. Li, M. Liu, G. Q. Lu and H. M. Cheng, *Angew. Chem., Int. Ed*. 2008, **47**, 373.
56 L. Bao, J. Zang and X. Li, *Nano Lett*. 2011, **11**, 1215.
57 T. Y. Wei, C. H. Chen, K. H. Chang, S. Y. Lu and C. C. Hu, Chem. Mater., 2009, 21, 3228